ACS Catalysis

Research Article

pubs.acs.org/acscatalysis

Synthesis and Evaluation of Cu-SAPO-34 Catalysts for Ammonia Selective Catalytic Reduction. 1. Aqueous Solution Ion Exchange

Feng Gao,* Eric D. Walter, Nancy M. Washton, János Szanyi, and Charles H. F. Peden*

Institute for Integrated Catalysis and Chemical & Materials Sciences Division, Pacific Northwest National Laboratory, P.O. Box 999, Richland, Washington 99352, United States

ABSTRACT: SAPO-34 molecular sieves are synthesized using various structure directing agents (SDAs). Cu-SAPO-34 catalysts are prepared via aqueous solution ion exchange (IE). Catalysts are characterized with surface area/pore volume measurements, temperature programmed reduction (TPR), electron paramagnetic resonance (EPR), and nuclear magnetic resonance (NMR) spectroscopies. Catalytic properties are examined using standard ammonia selective catalytic reduction (NH_3−SCR) and ammonia oxidation reactions. During solution IE, different SAPO-34 samples undergo different extent of structural damage via irreversible hydrolysis. Si content within the samples (i.e., Al−O−Si bond density) and framework stress are key factors that affect irreversible hydrolysis. Even using very dilute Cu acetate solutions, it is not possible to generate Cu-SAPO-34 samples with only isolated Cu^{2+} ions. Small amounts of CuO_x species always coexist with isolated Cu^{2+} ions. Highly active and selective Cu-SAPO-34 catalysts for NH_3-SCR are readily generated using this synthesis protocol, even for SAPO-34 samples that degrade substantially during solution IE. High-temperature aging is found to improve the catalytic performance. This is likely due to reduction of intracrystalline mass-transfer limitations via formation of additional porosity in the highly defective SAPO-34 particles formed after IE.

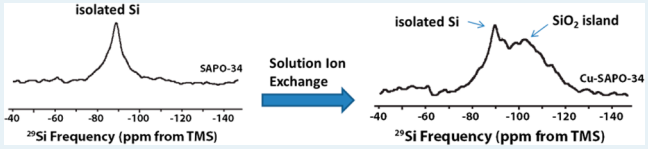

KEYWORDS: *selective catalytic reduction, chabazite, SAPO-34, Cu-SAPO-34, diesel engine, emission control, NO_x*

1. INTRODUCTION

For the past 15 years or so, the catalysis community has been addressing the significant challenge of reducing NO_x under the highly oxidizing (*lean-burn*) conditions encountered in the exhaust of diesel-powered vehicles. NO_x storage-reduction (NSR) and selective catalytic reduction (SCR) are leading NO_x emission control techniques for such lean-burn diesel engines.[1−6] In the past 2 or 3 years, SCR of NO_x with ammonia using metal-exchanged small-pore molecular sieves with a Chabazite (CHA) structure, for example, Cu-SSZ-13 and Cu-SAPO-34, has been implemented as part of the emission control systems for diesel passenger vehicles and light- and medium-duty trucks in the U.S. and Europe.[7,8] In 2010, we published the first open-literature paper describing the enhanced performance of Cu-SSZ-13 relative to Cu-beta and Cu-ZSM-5 in NH_3−SCR.[9] Subsequently, there have been a dozen or so publications that have addressed catalytic performance,[10−15] the nature of the Cu moieties,[15−22] Cu ion locations,[15−18] Cu loading effects,[14,15] among other issues[23] for the Cu-SSZ-13 catalysts. In contrast, the Cu-SAPO-34 catalysts have been much less studied.[10,20,24−27] Yet, the concept of metal ion-exchanged silicoaluminophosphate as thermally stable deNO_x catalysts dates back more than a decade.[28−31]

A typical diesel emission control system using SCR also includes a diesel oxidation catalyst (DOC) to treat unburned hydrocarbons and CO, and a diesel particulate filter (DPF) to trap particulate matter (PM). The DPF must be periodically heated to high temperatures (>650 °C) to burn off the trapped PM. Since the SCR catalyst bed and the DPF are closely placed in the emission control system, high hydrothermal stability is critical for practical SCR catalysts. H-SSZ-13 itself has rather limited hydrothermal stability and SCR activity. Sufficient amount of Cu^{2+} ions must be incorporated into extra-framework positions to enhance both hydrothermal stability and SCR activity.[10,16] The formation of Cu-SSZ-13 catalysts, via traditional solution ion exchange (IE), is rather straightforward.[9−17] On the other hand, SAPO-34 is a very refractory material, and the crystal structure maintains as high as 1000 °C even in the presence of humidity.[32] In this sense, the main purpose of Cu incorporation into SAPO-34 is to enhance SCR activity. However, Cu-SAPO-34 formation from solution IE is far from trivial because of the facile hydrolysis of SAPO-34 in aqueous solutions.

Upon removal of the structure directing agents (SDA), the SAPO-34 structure has long been known to be sensitive to humidity at ambient conditions.[33,34] From ^{29}Si MAS NMR, X-ray diffraction (XRD), and IR studies, Vomscheid et al. suggested that hydrolysis was due to Si−O−Al bond opening caused by H_2O attack, disturbing both long- and short-range order of the structure. This process has been found to be largely reversible where ordered material can be regenerated by removal of water at 150 °C.[33,34] However, repeated hydration-dehydration cycles and long-term storage (up to years) indeed cause irreversible damage.[34] On this basis, it is rather likely that

Received: June 20, 2013
Revised: July 31, 2013
Published: August 1, 2013

irreversible hydrolysis can be much more severe when SAPO-34 is dispersed into liquid water, a situation encountered during solution IE. This important issue, unfortunately, has not been addressed in detail before, and very few publications present surface area and pore volume changes prior to and after solution IE.[31,35,36] In one study, Frache et al. performed IE in a copper acetate solution ($[Cu^{2+}]$ = 0.1 M) at 50 °C for 5 h. The Cu-SAPO-34 thus generated only has a surface area of 21 m^2/g (note that pure SAPO-34 typically has a surface area >500 m^2/g).[31] Clearly, irreversible hydrolysis was extremely severe in this case. In studies by Akolekar et al., IE was carried out in a 0.014 M copper acetate solution at 75 °C for 4 h. In this case, the total surface area dropped from 615 to 324 m^2/g and the micropore volume dropped from 0.25 to 0.14 cm^3/g during IE.[35,36]

As has already been known, SAPO-34 can be synthesized hydrothermally using a vast number of organic and inorganic Al and Si sources and SDAs. In summary, the following parameters play important roles in affecting the properties of synthesized SAPO-34:[34,37−40] (1) the SDA chosen; (2) the Al and Si sources chosen; (3) the molar ratios of Si/Al/P/SDA of the gel; (4) reaction temperature; (5) reaction time, and others. Among these, SDAs play decisive roles in affecting Si distribution and framework charge density, while the choice of inorganic Al and Si sources and maintaining continuous stirring during synthesis are keys to form products with high crystallinity. In this study, we synthesized SAPO-34 samples using various SDAs and performed IE on these samples to generate Cu-SAPO-34 catalysts. We further characterized these catalysts with temperature-programmed reduction (TPR), nuclear magnetic resonance (NMR), and electron paramagnetic resonance (EPR) spectroscopies, and surface area/pore volume measurements, and evaluated their catalytic properties using standard NH_3−SCR and nonselective NH_3 oxidation reactions. The aim of this paper is to elucidate the causes of irreversible hydrolysis of SAPO-34 during solution IE, and to identify key factors in synthesizing highly active Cu-SAPO-34 for NH_3−SCR.

2. EXPERIMENTAL SECTION

2.1. Catalyst Synthesis. SAPO-34 zeolites were synthesized hydrothermally using triethylamine (TEA), morpholine (MOR), and 1/1 mixtures of MOR/TEA as SDAs, 85% *o*-phosphoric acid as the P source, aluminum hydroxide as the Al source, and fumed silica as the Si source. Poly(ethylene glycol), PEG-400, was also used as a crystal growth inhibitor (CGI) during synthesis to generate uniform and small (<5 μm) particles.[41] All chemicals were purchased from Sigma-Aldrich with purity of reagent grade or better. Synthesis gel composition was the following: 1 Al_2O_3: 0.85 P_2O_5: 1.0 SiO_2: 3 SDA: 0.2 PEG-400: 60 H_2O. After preparation under vigorous stirring at ambient temperature, the gel was sealed into a Teflon-lined stainless steel autoclave. Thereafter, the autoclave was buried inside a salt bath on top of a hot plate stirrer to carry out hydrothermal synthesis at 200 °C for 30 h. This setup allows continuous stirring during synthesis, a step critical for generating SAPO-34 with uniform size distribution and high crystallinity. After synthesis, SAPO-34 was separated from the mother liquid via centrifugation and washed with deionized water for 3 times. Finally, the zeolite powders were dried at 120 °C under flowing N_2 and calcined in air at 600 °C for 5 h. The materials thus generated are in hydrogen form, that is, H-SAPO-34.

To form Cu-SAPO-34, H-SAPO-34 was subjected to a two-step IE process. First, an IE step was applied using an excess amount of 0.1 M NH_4NO_3 at 50 °C for 1 h to generate NH_4−SAPO-34. Centrifugation separation and washing cycles were applied thereafter. Second, NH_4−SAPO-34 was exchanged with 0.01 M $Cu(OAc)_2$ at 50 °C for 1 h to generate Cu-SAPO-34. The amount of the $Cu(OAc)_2$ solution used, assuming complete Cu exchange, allows ∼6.4 wt % Cu loading in the final product. Again, Cu-SAPO-34 was separated, washed, and dried at 120 °C and then calcined at 600 °C for 5 h prior to characterization and reaction tests.

2.2. Catalyst Characterization. Composition of the SAPO-34 samples was determined with Inductively Coupled Plasma Atomic Emission Spectroscopy (ICP-AES) conducted at Galbraith Laboratories (Knoxville, TN, U.S.A.). Prior to measurements, the samples were partially dehydrated at 150 °C for 2 h in vacuum to remove adsorbed moisture. Brunauer−Emmett−Teller (BET) surface areas and micropore volumes of the SAPO-34 and Cu-SAPO-34 samples were measured with a Quantachrome Autosorb-6 analyzer. Prior to analysis, the samples were dehydrated under vacuum overnight at 250 °C. Temperature-programmed reduction (TPR) was performed on a Micromeritics AutoChem II analyzer. After purging the hydrated samples (samples stored in air and saturated with moisture) with pure N_2 at 10 mL/min at room temperature for 30 min, TPR was carried out in 5% H_2/Ar at a flow rate of 30 mL/min. Temperature was ramped linearly from ambient to 800 °C at 10 K/min and H_2 consumption was monitored with a TCD detector. Powder XRD measurements were performed on a Philips PW3040/00 X'Pert powder X-ray diffractometer with Cu K_α radiation (λ = 1.5406 Å). Data were collected at 2θ ranging from 5° to 50° with a step size of 0.02°.

EPR experiments were conducted on a Bruker E580 X-band spectrometer equipped with a SHQE resonator and a continuous flow cryostat. Powder samples (∼10 mg) were contained in 4 mm OD quartz tubes that can be purged/treated with various gases, cooled with liquid N_2 and helium, and heated to ∼350 °C. During spectral acquisition, microwave power was 200 microwatts, and the frequency was 9.86 GHz. The field was swept 1500 G in 84 s and modulated at 100 kHz with a 5 G amplitude. A time constant of 20 ms was used.

Nuclear magnetic resonance (NMR) experiments were performed on powder samples either as obtained (ambient) or after evacuation at 10^{-3} Torr and 150 °C for 12 h (partially dehydrated), and all experiments were conducted under a dry N_2 atmosphere. ^{27}Al and ^{31}P direct polarization (DP) experiments were carried out on a Varian VNMRS system operating at 14.1 T utilizing a 4 mm TR probe operating in DR mode. Direct polarization experiments with ^{1}H decoupling were conducted utilizing a ^{1}H frequency of 599.8517, continuous wave decoupling fields of 45 kHz for both ^{27}Al and ^{31}P, and ^{27}Al and ^{31}P frequencies of 156.3056 and 242.8129, respectively. Calibrated $\pi/20$ pulses of 0.50 us, spinning frequency of 15 kHz, a 50 kHz spectral window, 2048 complex points, and a 2 s pulse delay were utilized to acquire 512 time-averaged scans for ^{27}Al DP experiments. Time domain free induction decays were apodized with exponential functions corresponding to 200 Hz of Lorentzian line broadening prior to Fourier transformation. A $\pi/2$ pulse of 5.0 us, a spinning frequency of 15 kHz, 100 kHz spectral window, 4096 complex points, and a 240 s pulse delay were utilized to acquire 4 time-averaged scans for ^{31}P DP experiments. Time domain free induction decays were apodized with exponential functions

dx.doi.org/10.1021/cs4004672 | ACS Catal. 2013, 3, 2083−2093

Table 1. ICP-AES Results of Dehydrated SAPO-34 Samples Formed with Various SDAs

SDA	sample	Si (%)	Al (%)	P (%)	hexagonal unit cell composition (36T, 72O)
TEA	SAPO-34-TEA	4.3	21.5	16.6	$H_{\leq 3.7}Si_{3.7}Al_{19.3}P_{13.0}O_{72}$
MOR	SAPO-34-MOR	7.1	18.8	14.9	$H_{\leq 6.0}Si_{6.4}Al_{17.5}P_{12.1}O_{72}$
MOR/TEA (1/1)	SAPO-34-MIX	6.7	19.2	16.8	$H_{\leq 5.8}Si_{5.8}Al_{17.2}P_{13.0}O_{72}$

Table 2. BET and Micropore Surface Areas, Micropore Volume for the SAPO-34 and Cu-SAPO-34 Samples, and Cu Loadings for the Cu-SAPO-34 Samples from ICP and EPR

SDA	sample	BET surface area (m^2/g)	micro pore surface area (m^2/g)	micro pore volume (cm^3/g)	Cu loading from ICP (wt %)[a]	isolated Cu^{2+} from EPR (wt %)	normalized isolated Cu^{2+} (wt %)[b]
TEA	SAPO-34-TEA	480	436	0.220			
	Cu-SAPO-34-TEA	440	413	0.205	1.01	0.65	0.70
MOR	SAPO-34-MOR	549	532	0.268			
	Cu-SAPO-34-MOR	236	223	0.112	0.81	0.49	1.17
MOR/TEA (1/1)	SAPO-34-MIX	465	432	0.217			
	Cu-SAPO-34-MIX	123	91	0.046	0.63	0.44	2.08

[a]Estimated values in hydrated samples assuming these contain 15 wt % of H_2O. [b]Normalization based on pore volumes of SAPO-34 samples prior to IE.

corresponding to 100 Hz of Lorentzian line broadening prior to Fourier transformation. ^{29}Si DP experiments were carried out on a Varian VNMRS system operating at 20 T utilizing a 4 mm TR probe operating in DR mode. Direct polarization experiments with ^{1}H decoupling were conducted utilizing a ^{1}H frequency of 849.7299 and a continuous wave decoupling field of 50 kHz. A total of 640 time-averaged transients were acquired utilizing a $\pi/2$ pulse of 6.0 μs at a ^{29}Si frequency of 168.8018, spinning frequency of 10 kHz, a 50 kHz spectral window, 5024 complex points, and a 120 s pulse delay. Time domain free induction decays were apodized with exponential functions corresponding to 300 Hz of Lorentzian line broadening.

2.3. SCR and NH_3 Oxidation Reaction Tests. NH_3−SCR reaction kinetics were measured using a plug-flow reaction system described elsewhere.[15] Powder samples were pressed, crushed, and sieved (60−80 mesh) prior to use. For standard SCR, the feed gas contained 350 ppm NO, 350 ppm NH_3, 14% O_2, 2.5% H_2O, and balance N_2. NH_3 oxidation reaction was conducted in the same manner without NO_x. Stoichiometries for these reactions are shown below.

Standard SCR reaction:

$$4NH_3 + 4NO + O_2 = 4N_2 + 6H_2O$$

NH_3 oxidation reaction:

$$4NH_3 + 3O_2 = 2N_2 + 6H_2O$$

All of the gas lines were heated to over 100 °C to avoid water condensation. The total gas flow was 300 sccm, and the gas hourly space velocity (GHSV) was estimated to be ∼400,000 h^{-1} for a catalyst amount of 30 mg. Concentrations of reactants and products were measured by an online Nicolet Magna 560 FTIR spectrometer with a 2 m gas cell maintained at 150 °C.

For temperature-dependent steady-state reaction measurements, the catalysts were first activated in 14% O_2/N_2 flow for 1 h at 550 °C. Following which, NO, NH_3, and H_2O were added to the feed to start the SCR reaction. At each target temperature, a minimum waiting time of ∼45 min was applied to reach a steady-state. NO_x and NH_3 conversions were calculated based on the following equations:

$$NO_x\ \text{Conversion}\ \% = \frac{(NO + NO_2)_{inlet} - (NO + NO_2 + N_2O)_{outlet}}{(NO + NO_2)_{inlet}} \times 100$$

$$NH_3\ \text{Conversion}\ \% = \frac{(NH_3)_{inlet} - (NH_3)_{outlet}}{(NH_3)_{inlet}} \times 100$$

3. RESULTS

Table 1 presents the ICP-AES results for some of the synthesized SAPO-34 samples. (Note that the samples are denoted as SAPO-34-SDA (SDA = TEA or MOR) in the following except for the sample formed using mixed SDAs, which is denoted as SAPO-34-MIX.) Using these values, composition of the dehydrated hexagonal unit cells (containing 36 T and 72 O atoms) can be calculated; these are also presented in Table 1. The numbers of charge balancing protons for each unit cell, however, cannot be precisely determined. As will be discussed in more detail further below, only upper limits can be estimated.

Cu loadings for the Cu-SAPO-34 samples were also determined with ICP-AES. Recent studies by Li and co-workers[26,27] indicate, however, that regular IE on SAPO-34 with a Cu salt solution does not only generate isolated Cu^{2+} ion monomers, but also CuO_x species. We note that isolated Cu^{2+} ions are the only copper species found in Cu-SSZ-13, and these have been identified as the active sites for NH_3−SCR.[14−19] Both TPR and EPR were used by others to quantify isolated Cu^{2+} ions in Cu-SAPO-34.[27] In this study, we chose EPR for this purpose, and quantification was done by using standard solutions of Cu(II)-imidazole. As is well-known, Cu^{2+} ions tend to undergo autoreduction during vacuum and elevated temperature treatments to generate EPR silent Cu^+, and many chemisorbed molecules can modify the Cu^{2+} EPR signal intensity.[42,43] To precisely quantify the amount of isolated Cu^{2+} ions, the hydrated Cu-SAPO-34 samples were simply purged with dry N_2 at ambient without further treatments.

Table 2 presents BET and micropore surface areas of the SAPO-34 samples prior to and after IE. Interestingly, the extent of irreversible hydrolysis for different SAPO-34 samples was

dx.doi.org/10.1021/cs4004672 | ACS Catal. 2013, 3, 2083−2093

markedly different. The SAPO-34-TEA sample only experienced slight surface area and pore volume drop (~8%). In contrast, the SAPO-34-MOR and SAPO-34-MIX samples decomposed to a significant extent (~60% and ~80% of surface area and pore volume drop, respectively). Table 2 also presents total Cu loadings obtained from ICP-AES, and isolated Cu^{2+} ion loadings measured from EPR, for the Cu-SAPO-34 samples. We note that prior to ICP analysis, the Cu-SAPO-34 samples were partially dehydrated at 150 °C while EPR analysis was performed on hydrated samples. The ICP results shown in Table 2 were corrected assuming hydrated samples contain 15 wt % more H_2O than the partially dehydrated samples. This H_2O percentage was obtained by averaging weight losses of many samples heated to 150 °C for 2 h. By comparing the ICP-AES and EPR results, it is clear that only a portion of Cu in the Cu-SAPO-34 is present as isolated Cu^{2+} ion monomers; the rest are EPR silent species, for example, Cu-ion dimers and CuO_x clusters. We note first that this finding is consistent with a recent study by Xue et al., who also found multiple Cu-containing species in their Cu-SAPO-34 samples formed via solution IE.[27] Second, this behavior is markedly different from SSZ-13 where essentially only isolated Cu^{2+} ion monomers exist in Cu-SSZ-13 after solution IE.[14−19] It is expected that SAPO-34 samples with higher framework charge densities should accommodate more isolated Cu^{2+} ion monomers. This expected behavior, however, is not seen because of different degrees of irreversible hydrolysis for different SAPO-34 samples (From the Cu loadings shown in Table 2, it is seen that SAPO-34 samples with higher remaining pore volumes display higher Cu loadings). To make this comparison, normalized Cu^{2+} ion monomer loadings were calculated, and the results are shown in Table 2. The normalization was done based on micropore volumes of the corresponding SAPO-34 samples *prior to* IE. For example, the Cu-SAPO-34-MOR sample has an isolated Cu^{2+} ion loading of 0.49 wt %. However, the micropore volume for SAPO-34-MOR dropped from 0.268 to 0.112 cm^3/g during IE. Assuming no pore volume drop during IE, the normalized Cu^{2+} ion monomer loading becomes 1.17 wt % (i.e., 0.49 wt % × 0.268/0.112). From Table 2, the normalized Cu^{2+} ion monomer loading for Cu-SAPO-34-MIX is much higher than other samples, and this will be discussed in more detail below.

XRD patterns for the pairs of SAPO-34 and the corresponding Cu-SAPO-34 samples are displayed in Figure 1. There are a few important points worth addressing: (1) it is interesting to note that the XRD pattern for SAPO-34-TEA is less-well-defined indicating relatively low crystallinity. In contrast, the other two SAPO-34 samples are highly crystallized. Note that micro pores dominate on Chabazite molecular sieves; although SAPO-34-TEA shows less crystallinity, its pore volume is essentially the same as the much better crystallized SAPO-34-MIX. (2) For each SAPO-34 material, the XRD patterns prior to and after IE are fully consistent with the surface area/pore volume measurements shown in Table 2. For example, the SAPO-34-TEA sample underwent the least irreversible hydrolysis during IE and, indeed, the XRD patterns are essentially identical prior to and after IE. On the other hand, the SAPO-34-MOR/MIX samples experienced significant surface area and pore volume loss during IE and, indeed, a substantial drop in crystallinity was observed via XRD. Moreover, a "bump" is detected between 15 and 30° for the Cu-SAPO-34-MOR/MIX samples demonstrating formation of an amorphous phase upon SAPO-34 hydrolysis during IE. (3) Finally, the Cu-SAPO-34 yields during IE are also very

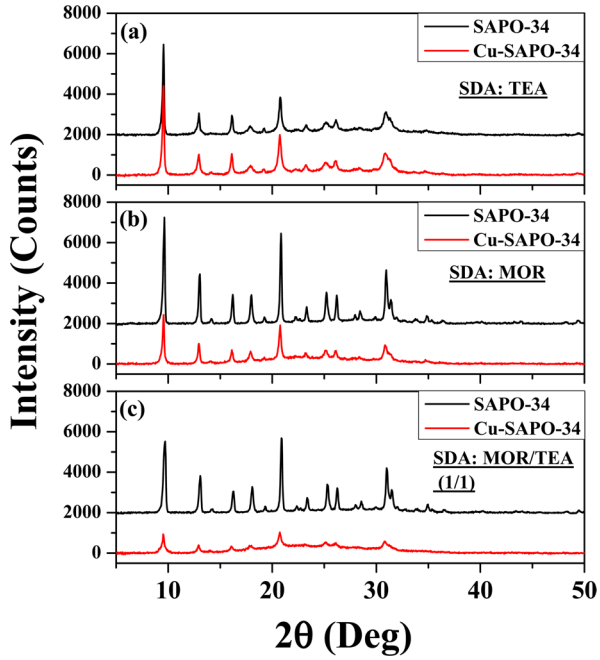

Figure 1. XRD patterns for SAPO-34 and Cu-SAPO-34 samples. SAPO-34 samples were formed using (a) TEA, (b) MOR, and (c) mixed (MOR/TEA = 1/1) SDAs.

different. The yield for Cu-SAPO-34-TEA is over 80%, the yield for Cu-SAPO-34-MOR is ~70%, while that for Cu-SAPO-34-MIX is merely ~50%. Besides the unavoidable weight loss during centrifugation separation, it appears, at least for the SAPO-34-MOR/MIX samples, that some SAPO-34 must have dissolved during IE.

To rationalize the dramatic differences in resistance to irreversible hydrolysis, solid-state NMR was used to monitor the differences in chemical environments of Al, P, and Si within different SAPO-34 samples. Figure 2a plots ^{27}Al MAS NMR spectra for hydrated and partially dehydrated SAPO-34 samples where partial dehydration was achieved by treating the samples in a vacuum oven held at 150 °C for 12 h. In the hydrated form, all three samples show features at 43 ppm assigned to tetrahedral Al (Al^{IV}), at ~10 ppm tentatively assigned to pentahedral Al (Al^{V}), and at −11 ppm attributed to octahedral Al (Al^{VI}).[40,44,45] For the SAPO-34-TEA sample, a weak shoulder peak is also found at ~65 ppm. The origin of this peak is less clear but seems very likely to be associated with distorted Al^{IV}, considering the fact that SAPO-34-TEA has the lowest crystallinity among the samples. Upon treatment at 150 °C, the Al^{V} and Al^{VI} features disappear demonstrating reversible dehydration.[33,34] The chemical shift of Al^{IV} at 38 ppm for dehydrated SAPO-34 is entirely consistent with previous studies.[33,34,40,44−46] Figure 2b presents the ^{31}P NMR data. For the hydrated samples, the chemical shift of tetrahedral P is observed at −28 ppm. Upon dehydration, it shifts to −29 ppm. Again, these chemical shifts are fully consistent with the literature.[33,34,40,44−46] Note that for the hydrated samples, a shoulder feature occurs at −15 ppm. This can be assigned to disordered P formed by SAPO-34 hydrolysis.[44] Again, the disappearance of this peak upon heat treatment demonstrates reversible hydration/dehydration. Overall, the ^{27}Al and ^{31}P NMR spectra for the three SAPO-34 samples appear to be rather similar, and the slow irreversible hydrolysis process

dx.doi.org/10.1021/cs4004672 | ACS Catal. 2013, 3, 2083−2093

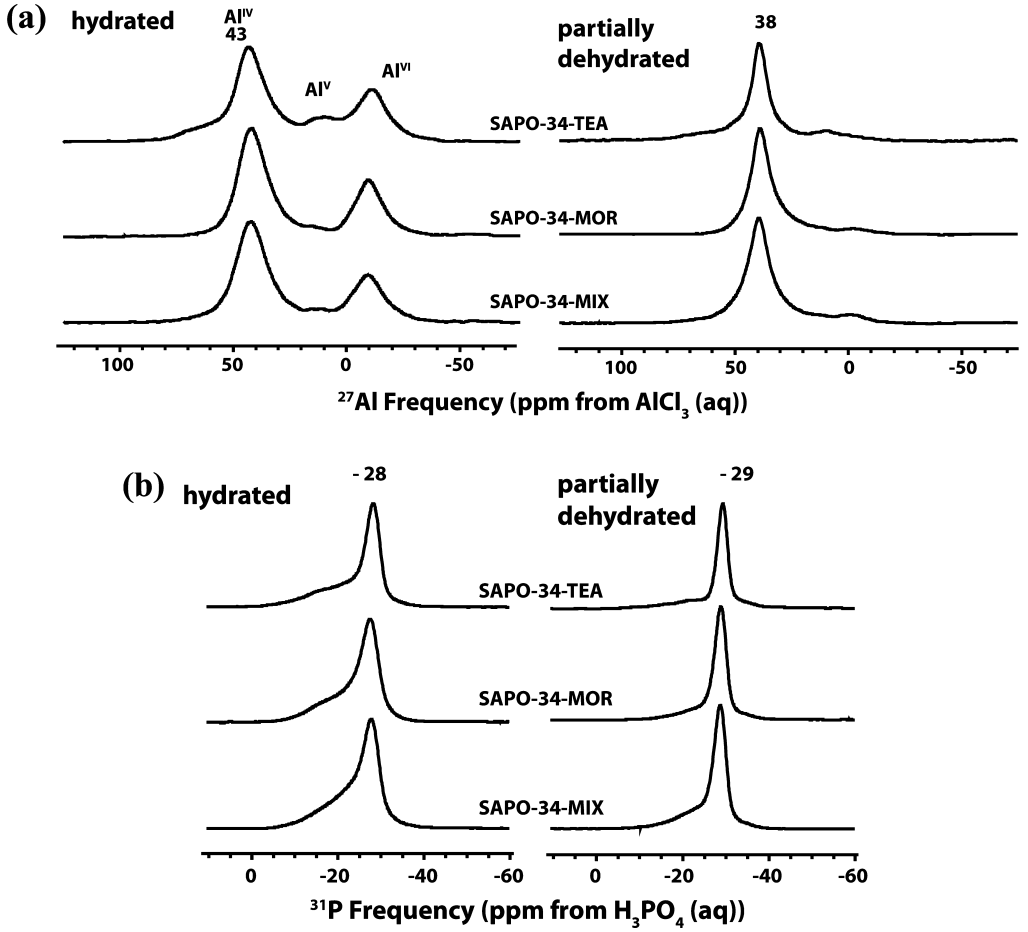

Figure 2. Solid state (a) ^{27}Al- and (b) ^{31}P NMR spectra for hydrated and partially dehydrated SAPO-34-TEA/MOR/MIX samples.

cannot be observed from a single hydration-dehydration cycle, as also demonstrated previously.[34]

The ^{29}Si NMR data for the hydrated SAPO-34 samples are depicted in Figure 3a. Spectra for the partially dehydrated samples were not acquired. In this case, marked differences are evident among the three samples. For the SAPO-34-TEA/MOR samples, features are observed at −89, −94, −99, −104, and −110 ppm. The −89 ppm peak is attributed to isolated Si, that is, Si(OAl)$_4$ species. The −94, −99, −104, and −110 ppm peaks are assigned to Si(OSi)$_n$(OAl)$_{4-n}$ (n = 1, 2, 3 and 4, respectively) moieties.[40,44,45] The formation of these latter features demonstrates the existence of various Si islands within these samples. Note also from Figure 3a that the percentage of isolated Si is lower in SAPO-34-TEA than that in SAPO-34-MOR. In contrast, the −89 ppm feature dominates for the SAPO-34-MIX sample indicating the majority of Si sites are isolated. Figure 3b presents ^{29}Si NMR spectra for the least stable SAPO-34-MIX prior to and after solution IE. Clearly, the dramatic growth of the peaks at chemical shifts of −94 ppm and lower after IE is fully consistent with the XRD and surface area/pore volume measurements, demonstrating extensive irreversible hydrolysis during IE.

It has been known for some time that, unlike the Cu-SSZ-13 catalysts which tend to deactivate gradually during hydrothermal aging, the Cu-SAPO-34 catalysts can become more active after aging. In particular, Wang et al.[26] reported this phenomenon in a recent study. These authors hydrothermally aged their catalysts at 750 °C for 12 h and realized higher activities, attributing this behavior to higher numbers of isolated Cu^{2+} ions generated during aging. In the present study, we thermally aged our samples at 800 °C for 16 h in air. Table 3 presents surface areas, pore volumes, and isolated Cu^{2+} loadings for the Cu-SAPO-34-TEA/MOR samples calcined at 600 °C for 5 h (same as in Table 2) and 800 °C for 16 h, respectively. Two points are worth addressing for these data: (1) calcination at 800 °C causes an ∼50% loss of surface area and pore volume for both samples, and (2) indeed, more isolated Cu^{2+} ions form during this high-temperature treatment.

Next, NH_3−SCR and NH_3 oxidation reaction results are presented for the 600 °C (5 h) and 800 °C (16 h) calcined samples. Figure 4a presents NO_x conversion as a function of temperature for the standard SCR reaction carried out at a moderate GHSV of 100,000 h^{-1} on Cu-SAPO-34-TEA (all other Cu-SAPO-34 samples show very similar behavior). Figure 4b presents the corresponding NH_3 conversion obtained during SCR reaction. Both samples are highly active for the target reaction with a light-off temperature at ∼200 °C. NO_x conversions higher than ∼85% maintain up to 550 °C. For the sample calcined at 600 °C, the NO_x and NH_3 conversion curves almost entirely overlap demonstrating nearly 100% selectivity in the target NH_3−SCR reaction. For the sample calcined at 800 °C, NO_x conversion slightly declines above ∼350 °C indicating some extent of nonselective NH_3 oxidation at high temperatures. In this case, NO_x conversion becomes limited by the availability of NH_3.[9,15] It is important to note that the sample calcined at 800 °C indeed displays higher SCR

dx.doi.org/10.1021/cs4004672 | ACS Catal. 2013, 3, 2083−2093

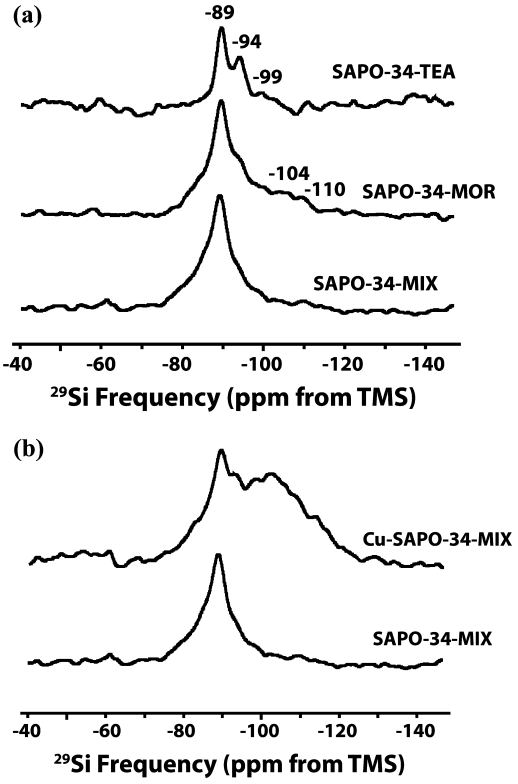

Figure 3. (a) Solid state ^{29}Si NMR for hydrated SAPO-34-TEA/MOR/MIX samples. (b) Comparison between solid state ^{29}Si NMR of SAPO-34-MIX and Cu-SAPO-34-MIX samples.

Table 3. BET and Micropore Surface Areas, Micropore Volume for the Cu-SAPO-34 Samples Thermally Treated at 600 and 800 °C

sample	thermal treatment condition	BET surface area (m^2/g)	micro pore surface area (m^2/g)	micro pore volume (cm^3/g)	isolated Cu^{2+} from EPR (wt %)
Cu-SAPO-34-TEA	600 °C, 5 h	440	413	0.205	0.65
	800 °C, 16 h	207	198	0.093	0.82
Cu-SAPO-34-MOR	600 °C, 5 h	236	223	0.112	0.49
	800 °C, 16 h	128	116	0.062	0.56

activity below 200 °C even though the surface area and pore volume are ∼50% lower. Figure 4c depicts nonselective NH_3 oxidation kinetics, also carried out at a GHSV of 100,000 h^{-1}. As expected based on their high selectivity in SCR, both samples display rather low activities for NH_3 oxidation. Note that the sample calcined at 800 °C shows higher oxidation activity, consistent with the slight SCR selectivity drop above 350 °C displayed in Figure 4a for this sample.

Recently we performed detailed reaction kinetics studies for NH_3−SCR and NH_3 oxidation on Cu-SSZ-13 catalysts with various Cu loadings.[15] For these experiments, we were able to conclude that the NH_3−SCR reaction is intracrystalline diffusion limited at low reaction temperatures, and this limitation becomes more severe at higher Cu loadings. In the same study, we also carried out experiments to identify kinetic regimes that are free of interparticle diffusion limitation. Basically, at GHSV ≥ 400,000h^{-1}, reaction temperature ≤200 °C, and NO_x conversion ≤20% conditions, interparticle limitations can be minimized for our Cu-CHA SCR catalysts. On this basis, NH_3−SCR reactions were carried out on Cu-SAPO-34 samples at GHSV = 400,000 h^{-1}. We note, however, that intracrystalline limitations cannot be removed by this means. Figure 5a plots NO_x conversion as a function of temperature. Note that although the samples do not deactivate under the reaction conditions, to obtain reproducible data at low reaction temperatures (where NO_x conversions are low), it is necessary to "activate" the samples at 550 °C first in oxygen for ∼1 h. Again, samples calcined at 800 °C display enhanced activities despite the fact that their surface area and pore volumes drop ∼50% (Table 3).

At low temperatures (e.g., ≤ 175 °C), the SCR reaction is relatively free from interparticle diffusion limitations and is also expected to be carried out only on isolated Cu^{2+} ion sites.[15−19] In principle, reaction rates can be normalized as turnover frequencies (TOF) in this case. However, as will be shown below, low-temperature kinetics are likely strongly affected by mass-transfer limitations. In this case, TOF is not particularly meaningful since the intrinsic activities for isolated Cu^{2+} sites are not properly probed. To obtain apparent reaction activation energies, NO_x conversions are used directly in the Arrhenius plots displayed in Figure 5b. Apparent reaction activation energies, thus acquired, are also tabulated in the figure. Interestingly, all three samples calcined at 600 °C prior to use show markedly different activation energies. Upon calcination to 800 °C, apparent SCR activation energies all dramatically increase.

4. DISCUSSION

4.1. SAPO-34 and Cu-SAPO-34 Synthesis. As has been mentioned in the Introduction, multiple factors affect SAPO-34 formation, but the most important ones are the choice of SDAs, choice of Al and Si sources, and stirring during synthesis. As is well-known, SDAs play three roles during the synthesis of molecular sieves, namely, structure directing, space filling, and charge compensating.[40] The charge compensating role for tetraethylammonium hydroxide (TEAOH), a SDA often used in SAPO-34 synthesis, is rather straightforward. Other amines and morpholine must be protonated to compensate the negative charges of the CHA framework. This leaves some uncertainty in determining the overall charge density of the CHA framework when these SDAs are used, as they may not all be protonated. The number of SDA molecules used to generate one SAPO-34 unit cell can be readily determined with thermogravimetric analysis (TGA). Based on previous studies, each hexagonal unit cell utilizes 3 TEAOH molecules, 3 TEA molecules, or 6 morpholine molecules during synthesis.[38,40] Assuming all SDA molecules are protonated, the framework charge for SAPO-34-MOR will be −6 per hexagonal unit cell, two times of that in SAPO-34-TEA. It has also been well-documented in the literature that Si substitution during SAPO-34 synthesis follows two mechanisms: single substitution of a tetrahedral P atom by a Si atom, or substitution of a P+Al pair with two Si atoms, where the former generates framework charge while the latter allows formation of charge neutral Si islands.[44−46] Overall, for a dehydrated SAPO-34 hexagonal unit cell formed with morpholine as SDA, the stoichiometry should be $H_6Si_6Al_{18}P_{12}O_{72}$ assuming (1) that all morpholine molecules protonate during synthesis and (2) no Si island formation. With the same assumptions, the unit cell formed with TEA should be

dx.doi.org/10.1021/cs4004672 | ACS Catal. 2013, 3, 2083−2093

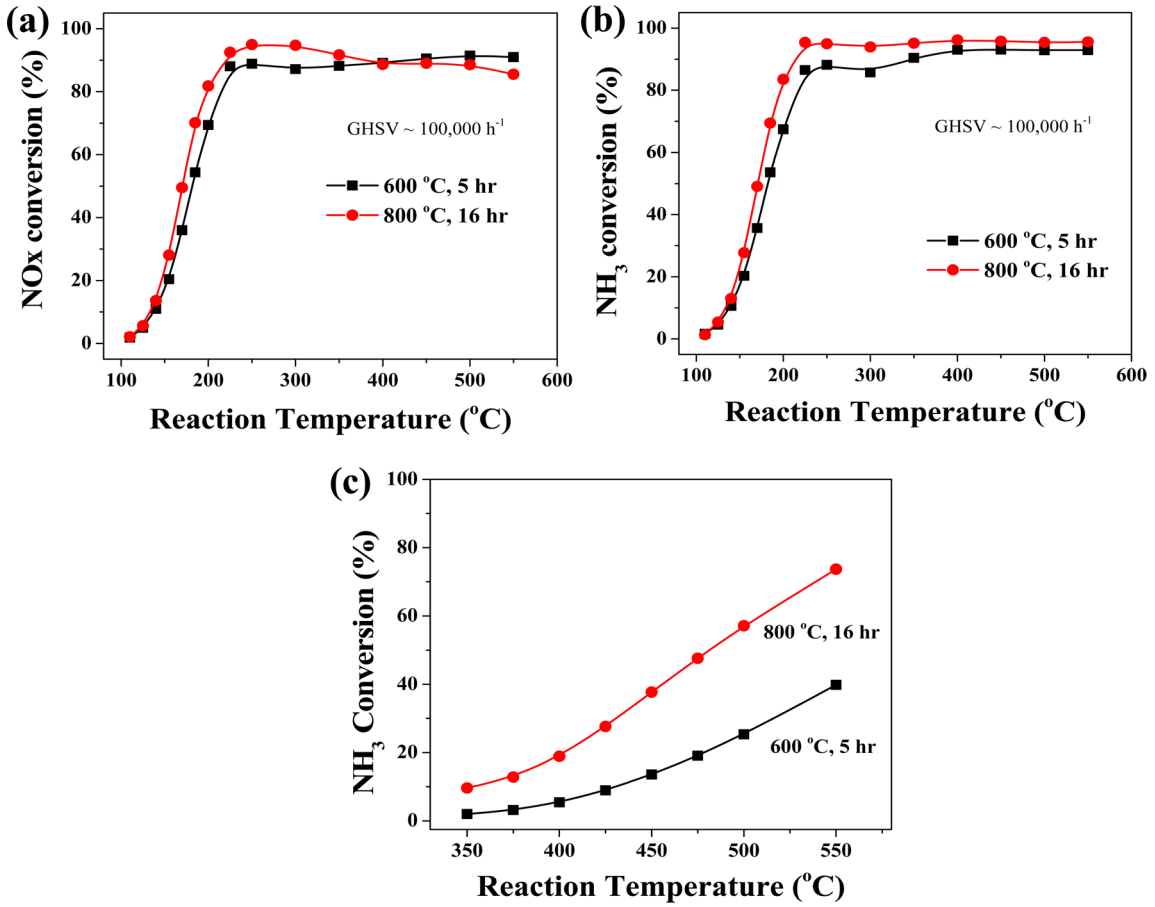

Figure 4. (a) NO_x conversion, and (b) NH_3 conversion, as a function of temperature on Cu-SAPO-34-TEA samples calcined at 600 (■) and 800 °C (●), respectively, in standard SCR. Reactant feed contains 350 ppm NO, 350 ppm NH_3, 14% O_2, 2.5% H_2O balanced with N_2. GHSV = 100,000 h^{-1}. (c) NH_3 conversion as a function of temperature on Cu-SAPO-34-TEA samples calcined at 600 (■) and 800 °C (●), respectively, in nonselective NH_3 oxidation. Reactant feed contains 350 ppm NH_3, 14% O_2, 2.5% H_2O balanced with N_2. GHSV = 100,000 h^{-1}.

$H_3Si_3Al_{18}P_{15}O_{72}$. The SAPO-34 sample compositions shown in Table 1, derived from ICP-AES, are reasonably close to these ideal compositions. This demonstrates the existence of more isolated Si sites compared with islanded Si sites within these samples, consistent with the ^{29}Si NMR data shown in Figure 3a. Importantly, by using different SDAs, one is able to form SAPO-34 samples with large differences in Si−O−Al bond densities.

One of the most interesting findings for the present study is the vast difference in resistance to irreversible hydrolysis for the SAPO-34 samples (Table 2 and Figure 1). Two causes are responsible for the difference. The first is the Si−O−Al bond density. As is known, the reversible hydrolysis of SAPO-34 is temperature dependent where at ambient conditions, H_2O attacks the Si−O(H)−Al bond causing its cleavage. H_2O molecules further interact with tetrahedral Al sites allowing their coordination numbers to rise. Above 100 °C, partial dehydration occurs. These processes are shown schematically in Figure 6a.[34] One of the best techniques to monitor the processes is ^{27}Al NMR as clearly demonstrated in Figure 2a. Furthermore, irreversibility involving condensation of silanol groups to form Si−O−Si bonds is evident from the ^{29}Si NMR data shown in Figure 3b. This process is schematically displayed in Figure 6b. It is conceivable that samples with higher Si−O−Al bond density undergo irreversible hydrolysis more readily. This process, however, proceeds very slowly when SAPO-34 is stored in air, a result that can be understood from steric arguments since reaction between silanol groups requires substantial deformation of the SAPO framework. However, it becomes much faster in aqueous solutions where the SAPO-34 structure can degrade dramatically within hours (Figure 3b). The second cause for the difference in irreversible hydrolysis is the CHA framework stress. This is generated via P substitution by Si; part of which comes from the framework charge that must be balanced by extra framework cations. One expects that SAPO-34 samples with more framework stress hydrolyze more readily. Again, SAPO-34-TEA has lower framework charge density than SAPO-34-MOR/MIX and, thus, framework stress is expected to be lower in the former samples. Furthermore, as shown in Figure 1, the SAPO-34-TEA sample has the lowest crystallinity, another indication that it should have the least framework stress among the SAPO-34 samples in this study. On the other hand, for the SAPO-34-MIX sample, since it was formed with mixed SDAs, framework stress is expected to be the highest. This follows since unit cells form around a variety of SDA combinations, thereby generating extra stress because of unit cell dimension variations. Overall, under identical solution IE conditions, the SAPO-34-TEA sample, because of its low Si−O−Al bond density and framework stress, only experienced ∼8% surface area and pore volume loss during IE because of irreversible hydrolysis. In contrast, the SAPO-34-MIX sample loses ∼80% of surface area and pore volume during IE because of its high Si−O−Al bond density and framework stress.

dx.doi.org/10.1021/cs4004672 | ACS Catal. 2013, 3, 2083−2093

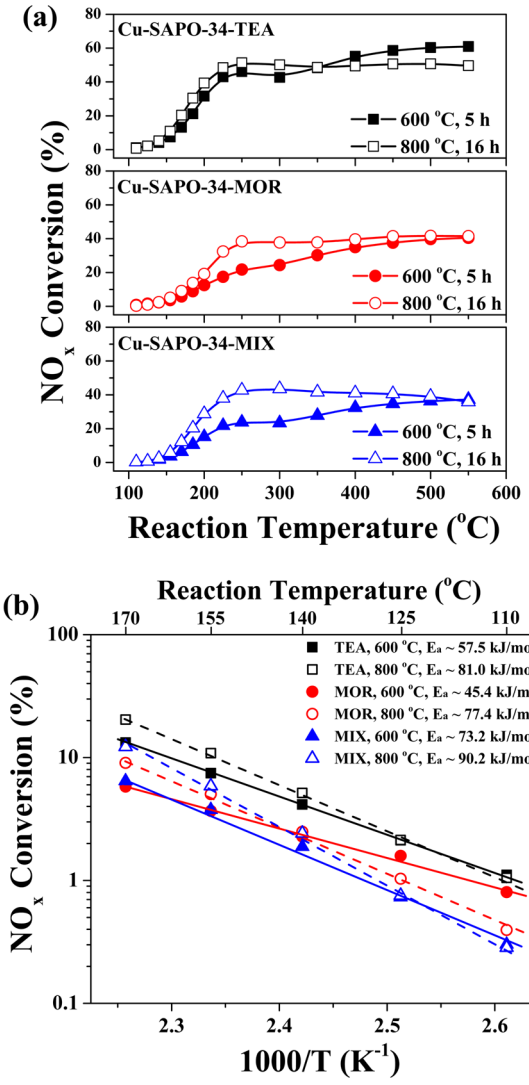

Figure 5. (a) NO_x conversion as a function of temperature on Cu-SAPO-34-TEA samples calcined at 600 (■) and 800 °C (□), on Cu-SAPO-34-MOR samples calcined at 600 (●) and 800 °C (○), and on Cu-SAPO-34-MIX samples calcined at 600 (▲) and 800 °C (Δ), respectively, in standard SCR. Reactant feed contains 350 ppm NO, 350 ppm NH_3, 14% O_2, 2.5% H_2O balanced with N_2. GHSV = 400,000 h^{-1}. (b) Arrhenius plots in the differential NO_x conversion regime. Note that the scale of the NO_x conversions is logarithmic. Apparent reaction activation energies are also tabulated.

Another interesting feature for SAPO-34 is that, during IE, besides isolated Cu^{2+} ions, other copper species (e.g., CuO_x clusters) also form. This is evidenced by the difference between total Cu loading derived from ICP analysis and isolated Cu^{2+} ion loading derived from EPR shown in Table 2. Note that (1) similar findings have been reported recently by others,[27] and (2) this behavior is different from that observed for the SSZ-13 CHA zeolite. For the latter, even at rather high IE levels, copper is predominately present as isolated Cu^{2+} ions.[15] In the present study, to avoid excessive irreversible hydrolysis and to avoid formation of Cu moieties other than isolated Cu^{2+} ions, dilute copper acetate solutions (0.01 M), very moderate temperatures (50 °C), and short contact times (1 h) were applied during IE. Even with these relatively mild conditions, we were unable to generate samples with only isolated Cu^{2+} ions. In principle, high IE levels are expected for SAPO-34 samples with high framework charge density. As shown in Table 2, the "normalized" isolated Cu^{2+} ion loadings assuming no irreversible hydrolysis, indeed reasonably reflect this trend. Especially the normalized Cu^{2+} ion loading for Cu-SAPO-34-MIX is substantially higher than other samples, consistent with the fact that SAPO-34-MIX has a high framework charge density (as evidenced from Figure 3a, this sample only has isolated Si species). Unfortunately, this sample also hydrolyzes irreversibly much more than the others. The other two Cu-SAPO-34 samples have rather similar Cu^{2+} ion loadings. Presumably, SAPO-34 unit cells with low framework charge density tend to be stable during IE while the ones with high framework charge density are more prone to hydrolysis leading to similar Cu^{2+} ion loadings balancing those unit cells that survive during IE. In this sense, it appears to not be possible to generate Cu-SAPO-34 catalysts with high isolated Cu^{2+} ion loadings from solution IE, whereas this is routinely achievable for Cu-SSZ-13. Similarly, isolated Cu^{2+} ions are not substantially more stable than CuO_x species because of the low framework charge density of the more stable SAPO-34 unit cells, and these tend to coexist in Cu-SAPO-34.

4.2. NH_3–SCR Reaction Kinetics. Cu-CHA catalysts have been shown to be very active and selective in NH_3–SCR.[9−15] This is again confirmed with our Cu-SAPO-34 catalysts (Figure 4). Furthermore, the hydrothermal stability for Cu-SAPO-34 is also expected to be outstanding (even better than Cu-SSZ-13) because of the refractory nature of SAPO materials. The particularly simple and well-defined structure of Cu-SSZ-13 is allowing long-standing issues of the catalytically active site for SCR in metal-exchanged zeolites to be addressed, and structure–activity relationships developed.[8,47] However, severe intracrystalline mass-transfer limitations for Cu-SSZ-13, due apparently to the small-pore opening structure of Chabazite, complicates such fundamental studies.[15] The present study demonstrates that Cu-SAPO-34 is more complex than Cu-SSZ-13. First, although SAPO-34 and SSZ-13 share the same CHA

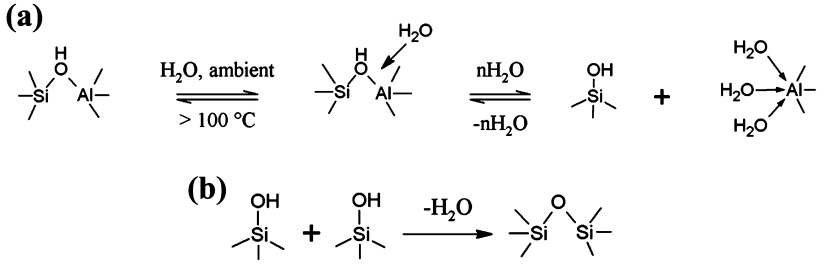

Figure 6. (a) Schematic of reversible hydrolysis of Si–O(H)–Al bond. (b) Schematic of irreversible hydrolysis of SAPO-34 via silanol group condensation.

dx.doi.org/10.1021/cs4004672 | ACS Catal. 2013, 3, 2083−2093

structure, the former has more complexity at an atomic level by, for example, having various Si/Al/P ratios and Si islands.[34,38,40] Second, Cu is predominately present as isolated Cu^{2+} ions in Cu-SSZ-13 while other Cu-containing moieties clearly coexist with isolated Cu^{2+} ions for Cu-SAPO-34 (Table 2). At low reaction temperatures (e.g., < 200 °C), there appears to be consensus that CuO_x species play no role and SCR reaction is carried out on isolated Cu^{2+} sites, or possibly $[Cu-O-Cu]^{2+}$ dimers.[6] As is well-known, isolated Cu^{2+} species are readily detectable and quantified with EPR; this is again confirmed by the current study. $[Cu-O-Cu]^{2+}$ dimer detection and quantification is more difficult. Qualitatively, the existence of large quantities of Cu-dimers leads to an EPR feature at half-field.[48] In the course of this study, EPR was applied to explore this half-field feature. No signal obviously stronger than the noise level was found in this region. Tentatively, we suggest that $[Cu-O-Cu]^{2+}$ dimers do not form in Cu-SAPO-34, and the only Cu-containing species are isolated Cu ions and CuO_x clusters.

One very interesting characteristic for Cu-SAPO-34 catalysts is that SCR activities even increase after rather harsh aging treatments. This is clearly demonstrated from the SCR kinetic data shown in Figures 4a, 4b, and 5a. Wang et al.[26] also realized this phenomenon and suggested that this is due to generation of more isolated Cu^{2+} ions during aging. Figure 7 presents EPR

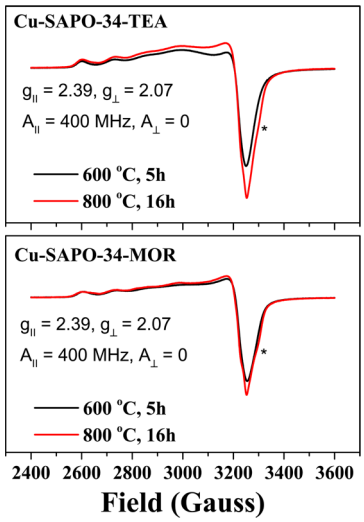

Figure 7. (a) EPR spectra for hydrated Cu-SAPO-34-TEA samples calcined at 600 (black line) and 800 °C (red line), respectively. g and A tensor values are also displayed adjacent to the spectra. (b) EPR spectra for hydrated Cu-SAPO-34-MOR samples calcined at 600 (black line) and 800 °C (red line), respectively. g and A tensor values are also displayed adjacent to the spectra.

spectra of hydrated Cu-SAPO-TEA and Cu-SAPO-34-MOR samples aged at 600 and 800 °C, respectively. Samples aged at 800 °C display slightly enhanced intensities at high field. This, indeed, demonstrates that more EPR active isolated Cu^{2+} ions form during aging (amounts listed in Table 3). Closer examination of the spectra on samples aged at 800 °C finds a weak shoulder feature at ~3300 G (marked with asterisks) in the high field and slight variation of the hyperfine features at low field. These subtle changes indicate slight decomposition of the Cu-SAPO-34 samples during the harsh thermal treatment at 800 °C. However, the spectra simulation results (displayed also in Figure 7) demonstrate that irrespective of the SDAs used to synthesize the SAPO-34 samples and the aging temperatures, g and A tensor values are identical for all samples studied. This indicates, at least under hydrated conditions, that all isolated Cu^{2+} ions are in very similar chemical environments. In other words, it does not appear likely that a high-temperature aging treatment generates special and highly active Cu^{2+} ion centers, although slight Cu^{2+} ion repositioning most certainly occurs during such a treatment. As shown in the middle panel of Figure 5a, at a reaction temperature of 250 °C, NO_x conversion roughly doubles on the Cu-SAPO-34-MOR sample aged at 800 °C compared with one aged at 600 °C. However, as displayed in Table 3, the sample aged at 800 °C only has a ~14% increase in isolated Cu^{2+} ion loading. Following the arguments immediately above, it is very unlikely that the main reason for SCR activity enhancement after aging at 800 °C is due to generation of more Cu^{2+} ions. In the following, we show that this is due mainly to elimination of intracrystalline (pore) diffusion limitations.

We have shown recently that for Cu-SSZ-13 catalysts, intracrystalline (pore) diffusion limitations play significant roles in the low-temperature kinetics.[15] The same situation is found for the Cu-SAPO-34 catalysts. For example, as displayed in Figure 5b, reaction activation energies for various samples calcined at 600 °C differ significantly even though the nature of the active Cu moieties is expected to be the same (i.e., isolated Cu^{2+} ions). Also by calcining the samples to 800 °C, reaction activation energies increase dramatically yet the nature of isolated Cu^{2+} ions is still likely the same (Figure 7). All of these experimental findings can be understood by invoking pore diffusion limitations, which we have discussed in detail previously.[15] In the following, this is discussed further.

Under pore diffusion limitation, true apparent reaction activation energies (E_t) are modified by a diffusion activation energy (E_D) term such that the observed apparent activation energy is given by $E_{ob} = (E_t + E_D)/2$. Since diffusion activation energies are typically small in the Knudsen diffusion regime (pore diameter > ~1 nm), in classic reaction kinetics studies, a drop of apparent activation energy to roughly a half is generally taken as a good indicator for the transition from a kinetically limited regime to a diffusion limited regime.[49] Note that pore diffusion limitations become more severe when (1) catalyst particle sizes increase and (2) pore dimensions decrease. In cases where catalysts have wide particle size and pore dimension distributions, precise determination of the rate-limiting kinetics can be difficult. Note also that in the intracrystalline diffusion regime (pore diameter <1 nm), the situation is further complicated by the fact that E_D may now become much higher than zero.[50,51] In the present study, irreversible hydrolysis during IE has two opposing effects on pore diffusion limitations: on the one hand, the formation of amorphous species blocks the CHA pore openings, thereby aggravating pore diffusion limitations. On the other hand, the partial dissolution of SAPO-34 decreases particle sizes and, therefore reduces such limitations. Note that the Cu-SAPO-34-TEA sample undergoes the least irreversible hydrolysis so that the two effects are expected to be minimal. Indeed, as shown in Figure 5b, this sample (calcined at 600 °C) has an E_a of 57.5 kJ/mol, rather similar to the apparent activation energy for Cu-SSZ-13 catalysts (~62 kJ/mol) measured under almost identical conditions.[15] The Cu-SAPO-34-MOR sample calcined at 600 °C displays the smallest E_a at 45.4 kJ/mol. Presumably, this latter sample experiences considerable pore blocking in IE. Interestingly, the Cu-SAPO-34-MIX catalyst, calcined at 600

dx.doi.org/10.1021/cs4004672 | ACS Catal. 2013, 3, 2083−2093

°C, shows a rather high E_a of 74.3 kJ/mol. According to the analysis above, this sample is expected to dissolve substantially during IE, and this is fully consistent with its low surface area and pore volume as shown in Table 2. This argument is further corroborated by the fact that, after the samples are calcined at 800 °C, all of them display enhanced SCR activity with markedly increased E_a (Figure 5), suggesting at least some reduction of pore diffusion limitations. During this high-temperature calcination, SAPO-34 particle sizes are not expected to decrease, although extra porosity within the particles can certainly form as a result of recrystallization of the highly defective structures generated during IE. This effect is expected to reduce pore diffusion limitations and enhance SCR activity. Indeed, there does not seem to be a more reasonable explanation to the reaction results shown in Figures 4 and 5 that, despite ∼50% of surface area and pore volume drop for the samples calcined at 800 °C, SCR activities markedly increase.

Finally, we think it useful here to compare our results to those recently published by Xue et al.,[27] who also applied solution IE to generate their Cu-SAPO-34 samples. On the basis of ICP analysis, EPR, and TPR, these authors suggested the coexistence of multiple Cu species. Our results are fully consistent with this general conclusion. However, the authors concluded that their samples also contain substantial amounts of Cu^+ species, based on their TPR analysis. We find this conclusion to be puzzling since Cu^+ species only form during Cu-SAPO-34 reduction, or under standard NH_3−SCR reaction conditions.[20,21] The as-prepared Cu-SAPO-34 catalysts stored under ambient conditions should not contain Cu^+ species. Note that an assumption about the presence and amount of Cu^+ species in ambient samples would affect quantitative estimates of various types of Cu species in the TPR results obtained by Xue et al. These authors also performed calculations (in their paper's Supporting Information) to suggest that intracrystalline diffusion does not limit SCR reaction for Cu-SAPO-34 catalysts. Specifically, they used the *Knudsen equation* to calculate average reactant velocities and further derived effective diffusivity on this basis. Finally, the effective diffusivity value was used to derive a Weisz−Prater factor smaller than 0.3, allowing the authors to rule out intracrystalline limitation. However, the average pore openings for the Chabazite materials (∼0.4 nm) are too small (i.e., beyond the Knudsen regime) for the Knudsen equation to apply.[50,51] Indeed, the effective diffusivity derived by the authors (1.3×10^{-5} m^2/s) is 3 orders of magnitude higher than that for CH_4 in H-ZSM-5 ($\sim 1 \times 10^{-8}$ m^2/s).[52] This is clearly not possible considering that (1) ZSM-5 has larger pore openings than Chabazite, and (2) NH_3−SCR reactants have similar kinetic diameters as CH_4. As such, the turnover frequencies reported by Xue et al.[27] are likely to be suspect.

5. CONCLUSIONS

(1) During the preparation of Cu-SAPO-34 catalysts via solution IE, SAPO-34 samples synthesized using different SDAs undergo very different degrees of irreversible hydrolysis. Al−O−Si bond density and framework stress are factors that are likely responsible for such a difference. In particular, SAPO-34 samples with high Al−O−Si bond density and framework stress experience more irreversible hydrolysis, and vice versa.

(2) Besides the preferred isolated Cu^{2+} ion species, CuO_x clusters also form during IE for all SAPO-34 materials studied here. This result can be understood from the relatively low charge density of the (more stable) CHA unit cells such that isolated Cu^{2+} ion species are not thermodynamically more stable than CuO_x clusters in SAPO-34.

(3) The low-temperature NH_3−SCR kinetics are controlled by intracrystalline mass-transfer limitations for the Cu-SAPO-34 catalysts. While the formation of amorphous species during IE may aggravate these limitations, partial dissolution of SAPO-34 may, in contrast, significantly reduce such limitations. High-temperature aging has been found to markedly reduce intracrystalline limitations, presumably by forming additional porosity in the highly defective SAPO-34 particles formed after IE.

AUTHOR INFORMATION

Corresponding Author

*E-mail: feng.gao@pnnl.gov (F.G.), chuck.peden@pnnl.gov (C.H.F.P.).

Notes

The authors declare no competing financial interest.

ACKNOWLEDGMENTS

The authors gratefully acknowledge the U.S. Department of Energy (DOE), Energy Efficiency and Renewable Energy, Vehicle Technologies Office, for the support of this work. The research described in this paper was performed at the Environmental Molecular Sciences Laboratory (EMSL), a national scientific user facility sponsored by the DOE's Office of Biological and Environmental Research and located at Pacific Northwest National Laboratory (PNNL). PNNL is operated for the U.S. DOE by Battelle Memorial Institute under contract number DE-AC05-76RL01830. Discussions with Drs. A. Yezerets, K. Kamasamudram, J. H. Li, and J. Y. Luo from Cummins, Inc. and H. Y. Chen and H. Hess from Johnson-Matthey are greatly appreciated.

REFERENCES

(1) Fridell, E.; Skoglundh, M.; Westerberg, B.; Johansson, S.; Smedler, G. *J. Catal.* **1999**, *183*, 196−209.
(2) Epling, W. S.; Campbell, L. E.; Yezerets, A.; Currier, N. W.; Parks, J. E., II *Catal. Rev.* **2004**, *46*, 163−245.
(3) Roy, S.; Baiker, A. *Chem. Rev.* **2009**, *109*, 4054−4091.
(4) Centi, G.; Perathoner, S. *Appl. Catal., A* **1995**, *132*, 179−259.
(5) Pârvulescu, V. I.; Grange, P.; Delmon, B. *Catal. Today* **1998**, *46*, 233−316.
(6) Brandenberger, S.; Krocher, O.; Tissler, A.; Althoff, R. *Catal. Rev.* **2008**, *50*, 492−531.
(7) Bull, I.; Xue, W. M.; Burk, P.; Boorse, R. S.; Jaglowski, W. M.; Koermer, G. S.; Moini, A.; Patchett, J. A.; Dettling, J. C.; Caudle, M. T. U.S. Patent 7,601,662, 2009.
(8) Gao, F.; Kwak, J. H.; Szanyi, J.; Peden, C. H. F. *Top. Catal.*, in press.
(9) Kwak, J. H.; Tonkyn, R. G.; Kim, D. H.; Szanyi, J.; Peden, C. H. F. *J. Catal.* **2010**, *275*, 187−190.
(10) Fickel, D. W.; D'Addio, E.; Lauterbach, J. A.; Lobo, R. F. *Appl. Catal., B* **2011**, *102*, 441−448.
(11) Schmieg, S. J.; Oh, S. H.; Kim, C. H.; Brown, D. B.; Lee, J. H.; Peden, C. H. F.; Kim, D. H. *Catal. Today* **2012**, *184*, 252−261.
(12) Kwak, J. H.; Tran, D.; Burton, S. D.; Szanyi, J.; Lee, J. H.; Peden, C. H. F. *J. Catal.* **2012**, *287*, 203−209.
(13) Ye, Q.; Wang, L. F.; Yang, R. T. *Appl. Catal., A* **2012**, *427−428*, 24−34.
(14) Kwak, J. H.; Tran, D.; Szanyi, J.; Peden, C. H. F.; Lee, J. H. *Catal. Lett.* **2012**, *142*, 295−301.
(15) Gao, F.; Walker, E. D.; Karp, E. M.; Luo, J. Y.; Tonkyn, R. G.; Kwak, J. H.; Szanyi, J.; Peden, C. H. F. *J. Catal.* **2013**, *300*, 20−29.

(16) Fickel, D. W.; Lobo, R. F. *J. Phys. Chem. C* **2010**, *114*, 1633−1640.
(17) Kwak, J. H.; Zhu, H. Y.; Lee, J. H.; Peden, C. H. F.; Szanyi, J. *Chem. Commun.* **2012**, *48*, 4758−4760.
(18) Korhonen, S. T.; Fickel, D. W.; Lobo, R. F.; Weckhuysen, B. M.; Beale, A. M. *Chem. Commun.* **2011**, *47*, 800−802.
(19) Deka, U.; Juhin, A.; Eilertsen, E. A.; Emerich, H.; Green, M. A.; Korhonen, S. T.; Weckhuysen, B. M.; Beale, A. M. *J. Phys. Chem. C* **2012**, *116*, 4809−4818.
(20) Kispersky, V. F.; Kropf, A. J.; Ribeiro, F. H.; Miller, J. T. *Phys. Chem. Chem. Phys.* **2012**, *14*, 2229−2238.
(21) McEwen, J. S.; Anggara, T.; Schneider, W. F.; Kispersky, V. F.; Miller, J. T.; Delgass, W. N.; Riberio, F. H. *Catal. Today* **2012**, *184*, 129−144.
(22) Szanyi, J.; Kwak, J. H.; Zhu, H. Y.; Peden, C. H. F. *Phys. Chem. Chem. Phys.* **2013**, *15*, 2368−2380.
(23) Ren, L. M.; Zhu, L. F.; Yang, C. G.; Chen, Y. M.; Sun, Q.; Zhang, H. Y.; Li, C. J.; Nawaz, F.; Meng, X. J.; Xiao, F. S. *Chem. Commun.* **2011**, *47*, 9789−9791.
(24) Wang, L.; Li, W.; Qi, G. S.; Weng, D. *J. Catal.* **2012**, *289*, 21−29.
(25) Martinez-Franco, R.; Moliner, M.; Franch, C.; Kustov, A.; Corma, A. *Appl. Catal., B* **2012**, *127*, 273−280.
(26) Wang, J.; Yu, T.; Wang, X. Q.; Qi, G. S.; Xue, J. J.; Shen, M. Q.; Li, W. *Appl. Catal., B* **2012**, *127*, 137−147.
(27) Xue, J. J.; Wang, X. Q.; Qi, G. S.; Wang, J.; Shen, M. Q.; Li, W. *J. Catal.* **2013**, *297*, 56−64.
(28) Ishihara, T.; Kagawa, M.; Hadama, F.; Takita, Y. *J. Catal.* **1997**, *169*, 93−102.
(29) Ishihara, T.; Kagawa, M.; Hadama, F.; Nishiguchi, H.; Ito, M.; Takita, Y. *Ind. Eng. Chem. Res.* **1997**, *36*, 17−22.
(30) Frache, A.; Palella, B.; Cadoni, M.; Pirone, R.; Ciambelli, P.; Pastore, H. O.; Marchese, L. *Catal. Today* **2002**, *75*, 359−365.
(31) Frache, A.; Palella, B. I.; Cadoni, M.; Pirone, R.; Pastore, H. O.; Marchese, L. *Top. Catal.* **2003**, *22*, 53−57.
(32) Watanabe, Y.; Koiwai, A.; Takeguchi, H.; Hyodo, S.; Noda, S. *J. Catal.* **1993**, *143*, 430−436.
(33) Vomscheid, R.; Briend, M.; Peltre, M. J.; Massiani, P.; Man, P. P.; Barthomeuf, D. *J. Chem. Soc., Chem. Commun.* **1993**, *6*, 544−546.
(34) Briend, M.; Vomscheid, R.; Peltre, M. J.; Man, P. P.; Barthomeuf, D. *J. Phys. Chem.* **1995**, *99*, 8270−8276.
(35) Akolekar, D. B.; Bhargava, S. K.; Foger, K. *J. Chem. Soc., Faraday Trans.* **1998**, *94*, 155−160.
(36) Akolekar, D. B.; Bhargava, S. K. *Appl. Catal., A* **2001**, *207*, 355−365.
(37) Bull, I.; Muller, U. European Patent 2269733, 2011.
(38) Alvaro-Munoz, T.; Marquez-Alvarez, C.; Sastre, E. *Catal. Today* **2012**, *179*, 27−34.
(39) Wilson, S.; Barger, P. *Microporous Mesoporous Mater.* **1999**, *29*, 117−126.
(40) Vomscheid, R.; Briend, M.; Peltre, M. J.; Man, P. P.; Barthomeuf, D. *J. Phys. Chem.* **1994**, *98*, 9614−9618.
(41) Venna, S. R.; Carreon, M. A. *J. Phys. Chem. B* **2008**, *112*, 16261−16265.
(42) Anpo, M.; Matsuoka, M.; Shioya, Y.; Yamashita, H.; Giamello, E.; Morterra, C.; Che, M.; Patterson, H. H.; Webber, S.; Ouellette, S.; Fox, M. A. *J. Phys. Chem.* **1994**, *98*, 5744−5750.
(43) Centi, G.; Perathoner, S.; Biglino, D.; Giamello, E. *J. Catal.* **1995**, *151*, 75−92.
(44) Tan, J.; Liu, Z. M.; Bao, X. H.; Liu, X. C.; Han, X. W.; He, C. Q.; Zhai, R. S. *Microporous Mesoporous Mater.* **2002**, *53*, 97−108.
(45) Shen, W. L.; Li, X.; Wei, Y. X.; Tian, P.; Deng, F.; Han, X. W.; Bao, X. H. *Microporous Mesoporous Mater.* **2012**, *158*, 19−25.
(46) Zibrowius, B.; Löffler, E.; Hunger, M. *Zeolites* **1992**, *12*, 167−174.
(47) Deka, U.; Lezcano-Gonzalez, I.; Weckhuysen, B. M.; Beale, A. M. *ACS Catal.* **2013**, *3*, 413−427.
(48) Chao, C. C.; Lunsford, J. H. *J. Chem. Phys.* **1972**, *57*, 2890−2898.
(49) Vannice, M. A. *Kinetics of Catalytic Reactions*; Springer: New York, 2005; p 60.
(50) Ruthven, D. W.; Post, M. F. M. *Stud. Surf. Sci. Catal.* **2001**, *137*, 525−577.
(51) Ruthven, D. M. *Stud. Surf. Sci. Catal.* **2007**, *168*, 737−785.
(52) Huang, H. Y.; Long, R. Q.; Yang, R. T. *Appl. Catal., A* **2002**, *235*, 241−251.